THE UNIVERSITY *of* EDINBURGH

Edinburgh Research Explorer

Prenatal disruption of blood–brain barrier formation via cyclooxygenase activation leads to lifelong brain inflammation

OPEN ACCESS

Prenatal disruption of blood–brain barrier formation via cyclooxygenase activation leads to lifelong brain inflammation

Qiuying Zhao[a] ⓘ, Weiye Dai[b] ⓘ, Hui Yu Chen[c], Russell E. Jacobs[a] ⓘ, Berislav V. Zlokovic[a], Brett T. Lund[d], Axel Montagne[e,f,1] ⓘ, and Alexandre Bonnin[a,1,2] ⓘ

Gestational maternal immune activation (MIA) in mice induces persistent brain microglial activation and a range of neuropathologies in the adult offspring. Although long-term phenotypes are well documented, how MIA in utero leads to persistent brain inflammation is not well understood. Here, we found that offspring of mothers treated with polyriboinosinic–polyribocytidylic acid [poly(I:C)] to induce MIA at gestational day 13 exhibit blood–brain barrier (BBB) dysfunction throughout life. Live MRI in utero revealed fetal BBB hyperpermeability 2 d after MIA. Decreased pericyte–endothelium coupling in cerebral blood vessels and increased microglial activation were found in fetal and 1- and 6-mo-old offspring brains. The long-lasting disruptions result from abnormal prenatal BBB formation, driven by increased proliferation of cyclooxygenase-2 (COX2; *Ptgs2*)-expressing microglia in fetal brain parenchyma and perivascular spaces. Targeted deletion of the *Ptgs2* gene in fetal myeloid cells or treatment with the inhibitor celecoxib 24 h after immune activation prevented microglial proliferation and disruption of BBB formation and function, showing that prenatal COX2 activation is a causal pathway of MIA effects. Thus, gestational MIA disrupts fetal BBB formation, inducing persistent BBB dysfunction, which promotes microglial overactivation and behavioral alterations across the offspring life span. Taken together, the data suggest that gestational MIA disruption of BBB formation could be an etiological contributor to neuropsychiatric disorders.

inflammation | blood–brain barrier | pregnancy | fetal programing | cyclooxygenase

It is well established that inflammation during fetal development increases risk for neurological disorders later in life. Despite a lack of clear mechanistic connection linking prenatal exposure to gestational maternal inflammation, sustained neuroinflammation, and long-term effects on offspring brain function, this concept of "fetal programming" is increasingly recognized as central to the onset of neurodevelopmental disorders, such as schizophrenia (1, 2). Although much less studied, recent data support the idea of prenatal inflammation also influencing the etiology of age-related neurodegenerative disorders. For instance, gestational maternal immune activation (MIA) triggered by the mismatched double-stranded RNA viral mimetic polyriboinosinic–polyribocytidylic acid [poly(I:C)] in mice was shown to increase levels of hippocampal amyloid precursor protein, alter Tau phosphorylation, induce microglia activation and reactive gliosis, and impair working memory in aging offspring, phenotypes indicative of Alzheimer's disease (AD)–like neuropathology (3, 4). Generally, activation of microglial cells in the adult offspring brain leading to a range of altered behaviors is observed across most MIA models (5–7). Yet, the developmental pathways whereby gestational MIA leads to sustained activation of brain microglial cells across the offspring life span are not fully understood.

There is growing evidence that systemic inflammation in adulthood alters cerebrovascular function, such as blood–brain barrier (BBB) permeability, leading to the leakage of immune mediators and toxic blood products into the brain parenchyma, which promotes sustained microglial activation and the progressive emergence of neuropathologies (8–10). A similar chain of events is particularly evident in AD and other dementias, where vascular dysfunctions leading to chronic brain inflammation directly contribute to the molecular pathology of disease (11–13). Although gestational MIA leads to microglial activation and sustained brain inflammation in the adult offspring, its impact on cerebrovascular development in utero and BBB function across the life span has not been investigated. To address this question, we induced immune activation by injection of the well-characterized immunostimulant poly(I:C) during pregnancy to study the immediate and long-term consequences on fetal and adult offspring BBB function in vivo. Live MRI studies reveal that gestational MIA induces long-lasting BBB hyperpermeability and cerebrovascular inflammation, effects consistent

Significance

This study demonstrates that maternal inflammation during pregnancy perturbs blood–brain barrier formation via cyclooxygenase activation in fetal microglia, leading to abnormal cerebrovascular function and chronic brain inflammation persisting across the offspring life span. Therefore, developmental disruption of blood–brain barrier formation could be an important etiological factor contributing to the pathology of neurodevelopmental disorders.

with observed decreased pericyte coverage of endothelial cells and increased endothelial expression of vascular cell adhesion molecule I (VCAM1). Tracking the developmental origins of these phenotypes, we found evidence of fetal BBB hyperpermeability using live MRI in utero and observed cellular disruptions as early as 48 h after gestational immune activation, suggesting the direct impact of inflammation on BBB development. We demonstrate pharmacologically and genetically that induction of cyclooxygenase-2 (COX2; *Ptgs2*) expression in microglia in the fetal brain is required for MIA-induced abnormal BBB development and subsequent long-term BBB leakage, offspring brain inflammation, and altered behaviors. Thus, maternal inflammation perturbs BBB formation at a critical time of fetal development and contributes to sustained brain inflammation and subsequent functional effects in adulthood.

Results

BBB Leakage in the Adult Offspring with Gestational MIA. First, to ensure that poly(I:C) injection at gestational day 13 (GD13) induces MIA, we quantified proinflammatory cytokines interleukin-6 (IL-6) and tumor necrosis factor-α (TNFα) and the chemokine monocyte chemoattractant protein-1 (MCP-1) concentrations in maternal serum 6 h after injection. The data show significant increase of IL-6 (3,346-fold increase over saline control), TNFα (35.6-fold), and C–C motif chemokine ligand-2 (also called MCP-1; 236.9-fold) protein concentration in the serum of poly(I:C)-injected mothers compared with saline controls (*SI Appendix*, Fig. S1*A*). At the dose used (10 mg/kg), poly(I:C) has no significant effect on maternal weight, time of birth, litter size, fetal sex ratio, and birth weight compared with saline-treated dams (*SI Appendix*, Fig. S1 *B–F*). To verify that gestational MIA triggered by poly(I:C) injection at GD13 induces brain parenchymal inflammation in the adult offspring (5, 7), we quantified the density and assessed the morphology of microglial cells in postnatal day 30 (PD30) brain. Consistent with previous studies, the number of Iba1+/ TMEM119+ microglial cells significantly increased in the PD30 MIA offspring cortex (Fig. 1 *B–D*), thalamus, and striatum (*SI Appendix*, Fig. S2 *A–C*). In MIA-exposed brains, these Iba1-expressing microglial cells display a decreased number of branches per cell compared with the control group in the cortex (Fig. 1*E*), thalamus, and striatum (*SI Appendix*, Fig. S2*D*), suggesting an activated phenotype. Other than brain parenchymal inflammation, altered anxiety- and memory-associated behaviors were observed in adult MIA offspring. We found decreased exploratory behavior in the open field test (OFT) in PD30 and PD180 MIA offspring (*SI Appendix*, Fig. S3 *C* and *E*), without change in overall motor activity (*SI Appendix*, Fig. S3 *D* and *F*), and a significant decrease in exploration preference of novel objects, a hippocampal activity–dependent behavior, in PD180 gestational MIA offspring compared with controls (*SI Appendix*, Fig. S3*G*). There were no significant effects of sex on behaviors in any of the treatment groups at both ages [effect of sex on OFT: PD30: $P = 0.64$, $F (1, 18) = 0.21$, $n = 5$ to 6 per sex; PD180: $P = 0.26$, $F (1, 13) = 1.35$, $n = 4$ to 5 per sex; effect of sex on exploratory preference: $P = 0.16$, $F (1, 12) = 2.14$, $n = 4$ per sex; two-way ANOVA with Tukey's post hoc test].

Brain parenchymal inflammation and altered behaviors have both been linked to BBB breakdown across the life span (10, 12, 14–16); therefore, we first used live imaging to investigate BBB integrity in gestational MIA offspring at PD30 and PD180. Strikingly, dynamic contrast-enhanced (DCE) MRI

analyses, which allow for the detection of subtle BBB permeability changes (11, 17), show that the BBB absolute blood to brain transfer constant (K_{trans}) is significantly increased in the cortex (36.6 ± 7.1%) (Fig. 1 *F* and *G*) of PD30 gestational MIA offspring compared with offspring of saline-treated mothers. Similar MIA-driven increases in K_{trans} were observed in the thalamus and striatum (*SI Appendix*, Fig. S3*A*), suggesting that MIA affects cerebrovasculature globally. BBB hyperpermeability was also observed in the PD180 cortex (K_{trans} increase of 41.9 ± 11.1% over saline controls) (Fig. 1*G*), thalamus, and striatum (*SI Appendix*, Fig. S3*B*) in the offspring of poly(I:C)-treated mothers. Consistent with behavioral measures, there were no significant differences between male and female offspring BBB permeability in saline and gestational MIA groups [effect of sex on K_{trans}: $P = 0.46$, $F (1, 20) = 0.56$, $n = 6$ per sex; two-way ANOVA with Tukey's post hoc test]. We next investigated if gestational MIA-induced BBB leakage leads to cerebrovascular inflammation, as it does in other models of BBB disruption in adults (18, 19). This was tested using molecular T2(transverse relaxation time)*-weighted (T2*w) MRI with intravenous injections of microparticles of iron oxide coupled to a monoclonal antibody targeting vascular cell adhesion molecule I [MPIO-aVCAM1 (20, 21)] in live PD30 offspring. MPIO-aVCAM1 is an antibody-based detection method to measure, via binding of the antibody moiety, changes in expression of VCAM1 on the luminal surface of blood vessels, as previously demonstrated (21). We measured a 74.1 ± 10.7% increase of cortical (and 94.6 ± 14.1% in the whole brain) MPIO-aVCAM1 signal in offspring from poly(I:C)- compared with saline-treated mothers (Fig. 1 *H* and *I*). In the gestational MIA group, MPIO-aVCAM1 signal intensity (SI) was also significantly increased in the thalamus and striatum (Fig. 1*I*). MPIO-aVCAM1 signal was localized exclusively to blood vessels (Fig. 1*H*), demonstrating a dramatic increase in vascular expression of this endothelial vascular inflammation marker throughout the brain. Furthermore, consistent with T2*w MRI data, we observe that the proportion of lectin+ endothelial cells in cortical vessels that are VCAM1+ is significantly increased in the PD30 gestational MIA offspring cortex compared with the saline group (Fig. 1 *J* and *K*). Similar observations were made in the thalamus and striatum (*SI Appendix*, Fig. S5).

Disruption of BBB Cellular Structure in the Adult Offspring with Gestational MIA. Previous studies in adult mice have clearly shown that pericyte loss leads to brain vascular damage and BBB leakage (15, 17, 22, 23). Therefore, to understand the cause of gestational MIA-induced BBB hyperpermeability, we quantified pericyte–endothelium coupling in PD30 offspring brains. To ensure the cellular identity of CD13+ pericytes, we labeled subsets of adjacent sections with an antibody directed against platelet-derived growth factor receptor-β (PDGFRβ). Immunostaining signals obtained with both markers overlap over extended cellular processes, and PDGFRβ cytoplasmic staining reveals the characteristic "bump-on-a-log" morphology of pericytes previously described (Fig. 1*N*) (24). Histologically, a significant decrease of pericyte coverage of endothelial cells (lectin+) was observed in the cortex using both markers (CD13 in Fig. 1 *L* and *M* and PDGFRβ in Fig. 1 *N* and *O*) of PD30 offspring of poly(I:C)-treated compared with saline-treated mothers; decreased coverage was also observed in the thalamus and striatum (*SI Appendix*, Fig. S4 *A–D*). The lectin+ vessels included in the quantification in both saline and MIA groups corresponded to capillaries (25), with an average diameter of ~3.5 mm (*SI Appendix*, Fig. S4*E*).
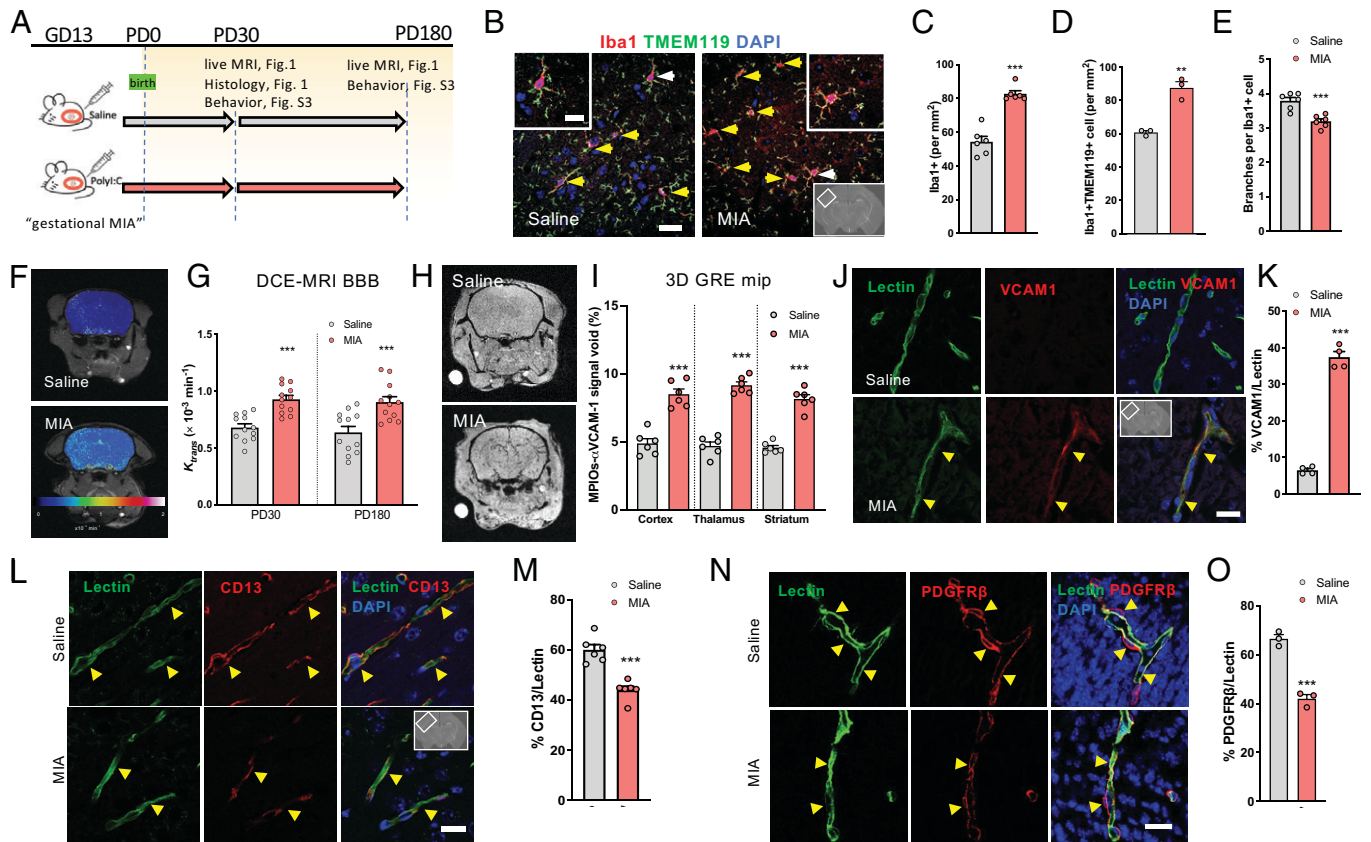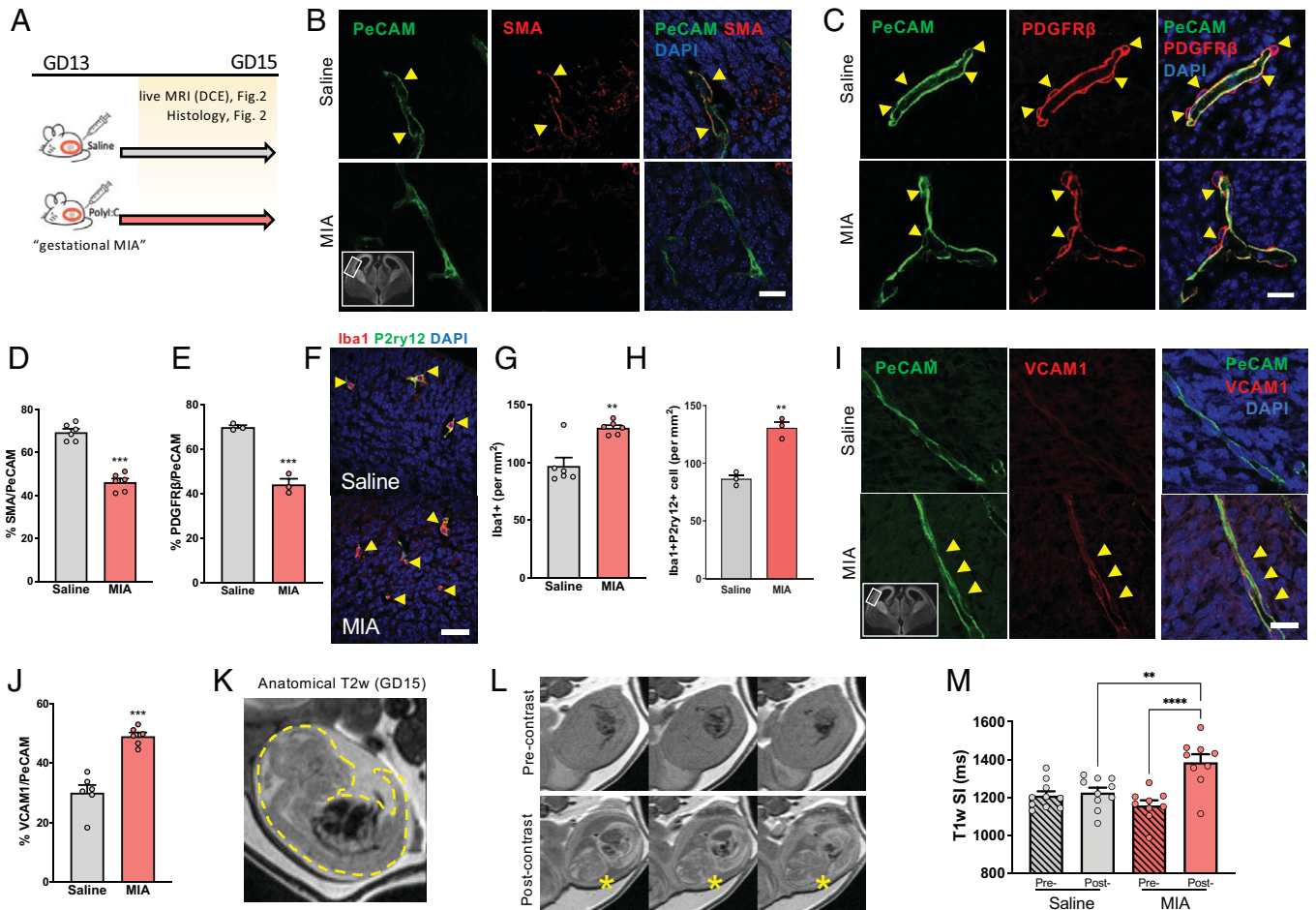
Fig. 1. Gestational MIA induces long-term BBB hyperpermeability in adult offspring. (*A*) Timed pregnant mice were injected with poly(I:C) ("gestational MIA") at GD13; outcomes were studied in PD30 and PD180 offspring. (*B*) Microglial cells markers Iba1 (red) and TMEM119 (green) and nuclear stain (DAPI, blue) in the cortex of the PD30 brain. Yellow arrows indicate Iba1+TMEM119+DAPI+ cells. (Scale bar, 50 μm.) (*Insets*) High-magnification views of Iba1+TMEM119+ microglial cells (white arrows). (Scale bar, 10 μm.) Quantification of Iba1+ cells (*C*), Iba1+TMEM119+ cells (*D*), and average branch number per Iba1+ cell (*E*) in saline and MIA cortex. (*F* and *G*) DCE MRI images and quantification of cortical BBB K_{trans} permeability in saline and MIA PD30 and PD180 offspring. (*H* and *I*) Molecular MRI of cerebrovascular inflammation using intravenous injections of MPIOs targeting VCAM1 shown by 3D GRE minimum intensity projection (mip) and quantification of the percentage of signal voids within the cortex, thalamus, and striatum of saline and MIA PD30 offspring. (*J*) Vascular inflammation marker VCAM1 (red) colocalization with endothelial cells (lectin+). Arrowheads point to VCAM1+lectin+ cells observed mainly in the MIA group. (Scale bar, 20 μm.) (*Inset*) Cortical location imaged. (*K*) Percentage of VCAM1/lectin colocalization in saline and MIA cortex. *n* = 4 mice per group. Colocalization of pericyte marker CD13 (red; *L*) and PDGFRβ (red; *N*) with endothelial cells (lectin+; green) in PD30 cortex of saline and MIA offspring (cortical region depicted in *L*, *Inset*). Arrowheads point to CD13/lectin and PDGFRβ/lectin staining overlap. Percentage of CD13/lectin (*M*) and PDGFRβ/lectin (*O*) signal overlap in saline and MIA cortex. (*C*, *E*, *I*, and *M*) *n* = 6 mice per group. (*G*) *n* = 12 mice per group. (*D* and *O*) *n* = 3 mice per group. Data represent mean ± SEM. (Scale bar, 20 μm.) **P < 0.01, two-tailed *t* test; ***P < 0.001, two-tailed *t* test.

Importantly, the density of lectin+ vessels in the cortex was not altered by MIA (*SI Appendix*, Fig. S4*F*), indicating that the K_{trans} increase reflects increased vessel permeability rather than change in density. Thus, the gestational MIA-induced decrease of pericyte–endothelial cells interactions leading to increased BBB permeability is already observed in the young adult offspring. These data overall show that the expected long-term microglial activation and behavioral deficits induced by gestational MIA are accompanied by chronic BBB hyperpermeability, cellular disruption, and cerebrovascular inflammation in the adult offspring brain.

Gestational MIA Acutely Alters BBB as Early as GD15. The fact that cellular and functional BBB disruptions are already observed in PD30 MIA offspring suggests that BBB development itself may have been compromised during the prenatal stages. Therefore, we sought to determine the prenatal onset of gestational MIA-induced BBB disruption. We investigated BBB formation at GD15, 48 h after MIA induction in pregnant mice (Fig. 2*A*). This is a time around which basic features of the fetal BBB emerge, such as the restriction of transcellular flow and the emergence of perivascular structures (coverage of the endothelial capillary wall by fetal pericytes) (26). We labeled fetal pericytes with two different markers to ensure their cellular identity: vascular

smooth muscle cells marker, SMA (smooth muscle actin; Fig. 2*B*), and PDGFRβ in subsets of adjacent sections (Fig. 2*C*). Immunostaining signals for both markers largely overlap over extended cellular processes (*SI Appendix*, Fig. S7), and like in the adult brain (Fig. 1*N*), PDGFRβ cytoplasmic staining reveals the characteristic bump-on-a-log morphology of pericytes (Fig. 2*C* and *SI Appendix*, Fig. S7) (24). Strikingly, both markers revealed a significant decrease of pericytes coverage of fetal blood vessels endothelial cells (platelet endothelial cell adhesion molecule-1; PeCAM+) in the fetal cortex (Fig. 2 *D* and *E*), thalamus (*SI Appendix*, Fig. S6 *A* and *C*), and striatum (*SI Appendix*, Fig. S6 *B* and *D*). The PeCAM+ vessels included in the quantification in both saline and MIA groups corresponded to capillaries, with an average diameter of ~4 μm (*SI Appendix*, Fig. S6*E*). Importantly, the density of PeCAM+ vessels in the cortex was not altered by MIA (*SI Appendix*, Fig. S6*F*). Despite changes in pericyte coverage of endothelial cells, we did not observe significant changes in tight junction markers Claudin-5 and ZO1 immunostaining density in GD15 fetal cortex from MIA vs. control groups (*SI Appendix*, Fig. S8). An increased number of P2ry12+/Iba1+ microglial cells was observed in GD15 fetal brain 48 h after gestational MIA (Fig. 2 *F–H*), as well as up-regulation of vascular inflammation

Fig. 2. Disruption of fetal BBB formation and cerebrovascular inflammation 48 h after MIA induction in utero. (*A*) Timed pregnant mice were injected with poly(I:C) (gestational MIA) at GD13; outcomes were studied in GD15 fetuses. Colocalization of pericyte markers SMA (red; *B*) and PDGFRβ (red; *C*), endothelial cells marker PeCAM (green) and nuclear stain DAPI (blue) in saline and MIA GD15 cortex (cortical region depicted in *B*, *Inset*). Arrowheads indicate SMA/PeCAM and PDGFRβ/PeCAM staining overlap. (Scale bars, 20 μm.) Quantification of SMA/PeCAM (*D*) and PDGFRβ/PeCAM (*E*) signal colocalization in GD15 cortex. (*F*) Microglial cells markers Iba1 and P2ry12 (arrowheads) in GD15 cortex. (Scale bar, 50 μm.) (*G* and *H*) Iba1+ cells and Iba1+P2ry12+ cells in saline and MIA cortex. (*I*) Cerebrovascular inflammatory marker/VCAM1 (red) and endothelial cells (PeCAM+; green) and nuclear stain DAPI (blue). Arrowheads indicate signal overlap. Cortical region depicted in *I*, *Inset*. (Scale bar, 20 μm.) (*J*) Quantification of VCAM1/PeCAM signal colocalization in GD15 cortex. (*D*, *G*, and *J*) n = 6 dams per group. (*E* and *H*) n = 3 dams per group and one fetal brain per dam. (*K*) Anatomical T2*w image of a live GD15 fetus (dotted lines) in a saline-treated dam. (*L*) Example of T1w pre–Gd-DTPA (*Upper*) and post–Gd-DTPA contrast (*Lower*) images in a poly(I:C)-treated pregnant mouse at GD15 (asterisks indicate the fetal brain postcontrast). (*M*) T1w SI reflecting Gd-DTPA distribution and thus, BBB integrity in saline and MIA GD15 fetal brains. n = 10 saline-treated dams, and n = 9 MIA-treated dams (one to three embryos per dam). Data are presented as mean ± SEM. (*D*, *E*, *G*, *H*, and *J*) **P < 0.01, ***P < 0.001, two-tailed *t* test. (*M*) **P < 0.01, ****P < 0.001, one-way ANOVA with Tukey's multiple comparison test.

marker VCAM1 expression in PeCAM+ endothelial cells (Fig. 2 *I* and *J*). These increases were observed in all regions of fetal brain investigated, including thalamus (*SI Appendix*, Fig. S9 *A* and *C*) and striatum (*SI Appendix*, Fig. S9 *B* and *D*). Such structural alterations of fetal BBB induced by gestational MIA suggest compromised permeability, which we tested functionally using live MRI in GD15 pregnant dams 48 h after poly(I:C) or saline injection. High-resolution abdominal T1-weighted (T1w) respiratory-gated sequences (Fig. 2 *K* and *L*) were used for quantitative measure of T1w signal intensities in different fetal compartments before and after maternal intravenous injection of paramagnetic gadolinium diethylenetriamine pentaacetic acid (Gd-DTPA) contrast. Remarkably, T1w scans demonstrate a significant increase of Gd signal within the fetal brain at GD15 in animals treated with poly(I:C) at GD13 (Fig. 2*M*). This suggests that pericyte–endothelial coupling deficits induced by gestational MIA lead to an increase in fetal BBB permeability to Gd-DTPA.

Overall, results show that within 48 h, gestational MIA induces abnormal fetal BBB maturation via decreased pericyte

coupling to fetal endothelial cells. This disruption of BBB maturation is associated with increased permeability to a small molecule (Gd-DTPA) and cerebrovascular inflammation.

Celecoxib Prevents Gestational MIA Effects on Fetal and Adult Offspring BBB Function. We next sought to identify inflammatory mediators of barrier disruption in the fetus. Based on their recognized involvement in mediating gestational MIA effects on offspring brain function (27, 28), we measured maternal blood serum and fetal brain protein concentrations of IL-6 and TNFα cytokines and MCP-1 chemokine at different time points after poly(I:C) injection. As mentioned earlier, maternal serum concentration of IL-6, TNFα, and MCP-1 increased dramatically 6 h after poly(I:C) injection, but values returned to control level by 28 and 48 h (Fig. 3*A* and *SI Appendix*, Fig. S1*A*). Interestingly, we did not detect any change in IL-6, TNFα, and MCP-1 protein tissue concentration in the fetal brain at any of those time points (Fig. 3*B*). There was, however, a significant increase of the inflammatory
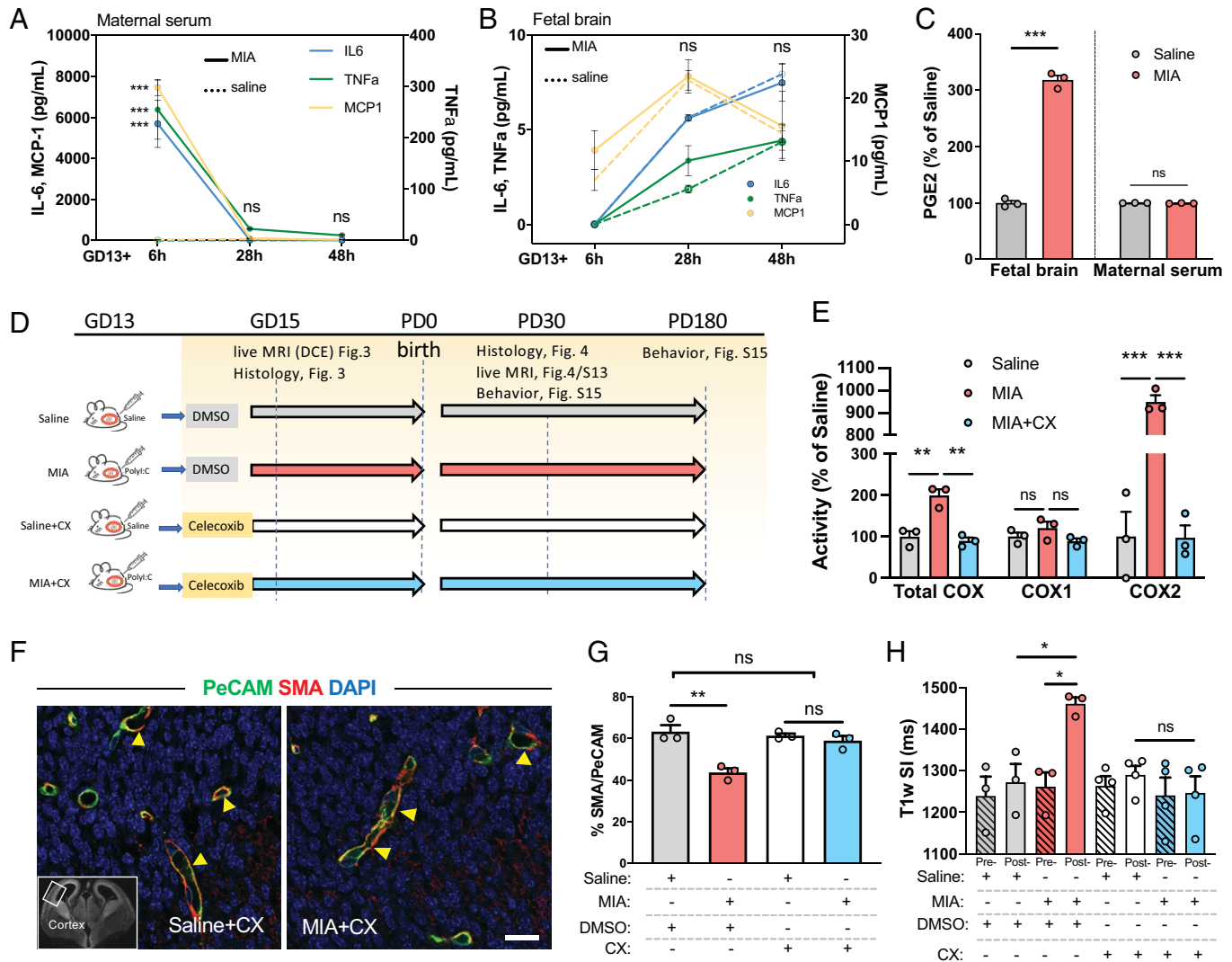
Fig. 3. The COX2 pathway is critical for gestational MIA effects on fetal BBB formation and function. Measures of (*A*) maternal serum and (*B*) fetal brain protein concentrations of proinflammatory cytokines IL-6, TNFα, and MCP-1 chemokine 6, 28, and 48 h after GD13 saline (dashed lines) or poly(I:C) injection (MIA; solid lines). (*C*) Measure of PGE2 tissue concentration in the whole fetal brain and maternal serum 28 h after maternal poly(I:C) injection. (*D*) Experimental scheme of COX2 blocking experiments. (*E*) Measure of total COX, COX1, and COX2 enzymatic activity in fetal brain 28 h after GD13 saline or poly(I:C) injection. (*F* and *G*) Representative images (*F*) and quantification (*G*) of endothelial (PeCAM+) and pericyte-like (SMA) colocalization in GD15 fetal cortex (nuclear marker DAPI, blue); dams received CX or vehicle (dimethylsulfoxide [DMSO]) 24 h after saline or MIA. Cortical region depicted in *F*, *Inset*. (Scale bar, 20 μm.) (*H*) Quantification (T1w SI) of tracer (Gd-DTPA) distribution into the fetal brain at GD15 in saline/MIA + vehicle (DMSO) and saline/MIA + CX groups. (*A–G*) n = 3 to 4 dams per group (one fetus per dam). (*H*) DMSO, n = 3 dams per group; CX, n = 4 dams per group. Data are presented as mean ± SEM. ns, not significant. *$P < 0.05$, one-way ANOVA with Tukey's multiple comparison test (*H*); **$P < 0.01$, two-way ANOVA with Bonferroni's multiple comparison test (*E*) and one-way ANOVA with Tukey's multiple comparison test (*G*); ***$P < 0.001$, two-way ANOVA with Bonferroni's multiple comparison test (*A* and *E*) and two-tailed *t* test (*C*).

mediator prostaglandin E2 (PGE2) in the fetal brain, but not maternal serum, 28 h post-MIA (Fig. 3*C*). PGE2 is a product of arachidonic acid metabolism by COX2 and mPGES1 enzymes, the former being highly inducible by inflammation (29, 30). Therefore, we hypothesized that COX2 activation in the fetal brain itself could be a mediator of gestational MIA effects on BBB maturation. To further test COX2 involvement in triggering gestational MIA effects in utero, we injected the specific COX2 inhibitor celecoxib (CX) into pregnant dams 24 h after MIA induction (Fig. 3*D*), when maternal inflammation itself has subsided (serum cytokines have returned to baseline) (Fig. 3*A*) but fetal brain PGE2 tissue concentration is still elevated (Fig. 3*C*). CX was shown to inhibit COX2 enzymatic activity and specifically down-regulate COX2 (but not COX1) expression in the N13 microglial cell line after immune stimulation (26). We measured the effect of MIA and CX on COX1 and COX2 enzymatic

activities in the fetal brain 28 h after MIA induction; COX1 activity was unaffected by MIA or CX treatment, whereas COX2 activity was significantly increased by MIA and returned to baseline within 4 h after CX treatment (Fig. 3*E*). We then measured the cellular and functional effects of CX on MIA-mediated disruptions of BBB function at GD15 (Fig. 3 *F–H*) and in the adult offspring (Fig. 4). Maternal CX injection prevented gestational MIA-induced PGE2 concentration increase in the fetal brain within 4 h after injection (116.6 ± 14.7%, $P = 0.816$, one-way ANOVA, compared with saline) and importantly, also prevented gestational MIA-induced pericyte–endothelium coverage deficit in the fetal cortex (Fig. 3 *F* and *G*), thalamus (*SI Appendix*, Fig. S10 *A* and *C*), and striatum (*SI Appendix*, Fig. S10 *B* and *D*). Maternal CX injection also blocked gestational MIA-induced increase in VCAM1 expression in fetal vessels in GD15 cortex (*SI Appendix*, Fig. S11 *A* and *B*), thalamus (*SI Appendix*, Fig. S11*C*), and
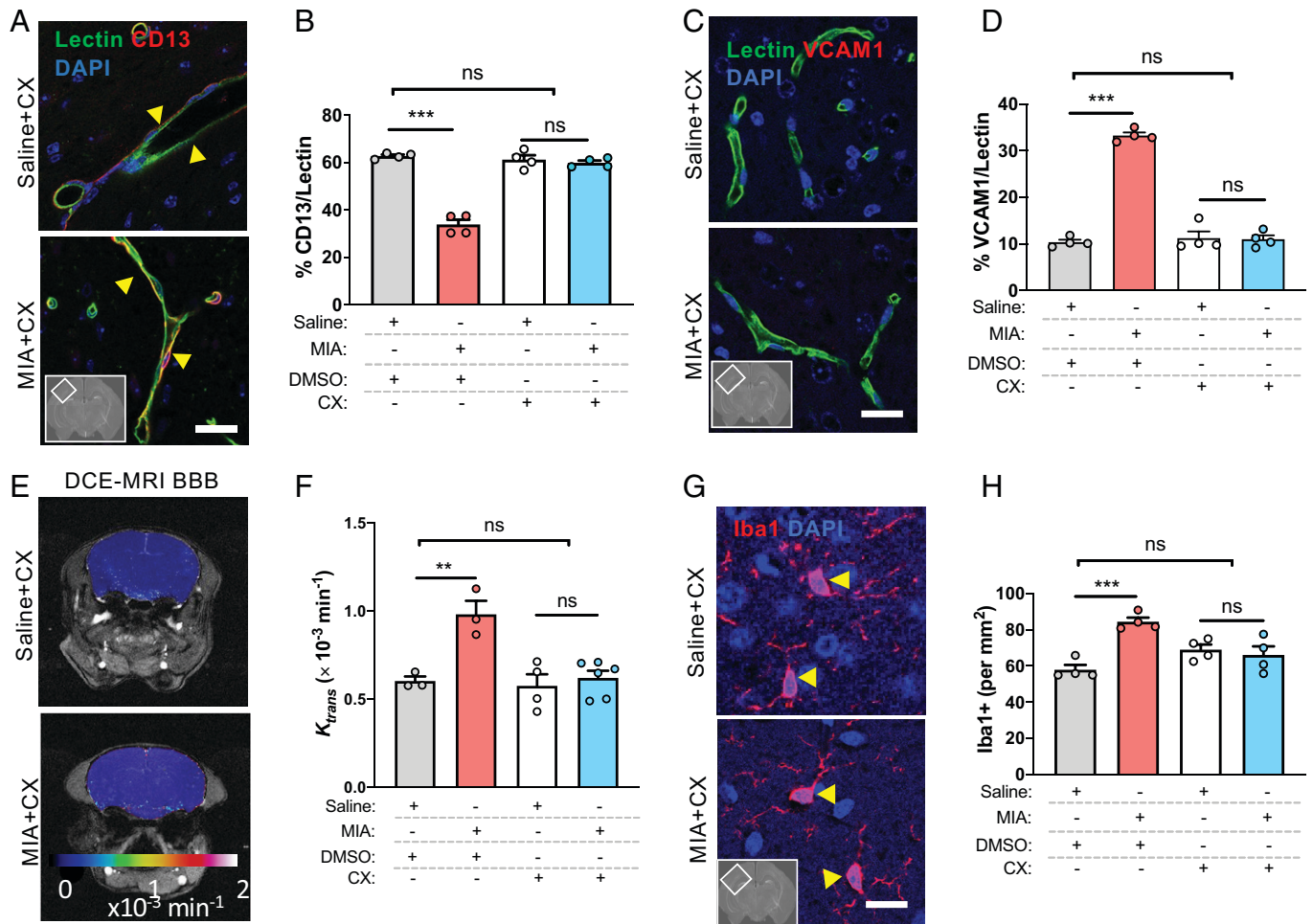
Fig. 4. Prenatal COX2 inhibition prevents MIA-induced BBB dysfunction in offspring. (A) Pericyte marker CD13 (red) overlaps with endothelial cell marker lectin (green) in the cortex of PD30 offspring born from mice treated prenatally with the COX2 inhibitor CX 24 h after saline or poly(I:C) (MIA) injection (blue, nuclear marker DAPI). Arrowheads point to areas of lectin/CD13 signal colocalization. Cortical region depicted in A, Inset. (Scale bar, 20 μm.) (B) Quantification of CD13/lectin signal overlap in the cortex PD30 offspring from mothers treated prenatally with saline, poly(I:C) (MIA), and vehicle (DMSO) or CX. (C) Vascular inflammation marker VCAM1 (red) and endothelial cell marker lectin (green) staining in the cortex of PD30 offspring born from mice treated prenatally with the COX2 inhibitor CX 24 h after saline or poly(I:C) (MIA) injection. Blue, nuclear marker DAPI. Cortical region depicted in C, Inset. (Scale bar, 20 μm.) (D) Quantification of VCAM1/lectin signal overlap in the cortex of PD30 offspring from mothers treated prenatally with saline, poly(I:C) (MIA), and vehicle (DMSO) or CX. (E) DCE MRI BBB K_{trans} images in PD30 offspring born from mothers treated with saline + CX and MIA + CX. (F) Quantification of cortical BBB K_{trans} permeability in PD30 offspring born from mice treated with saline or poly(I:C) (MIA) at GD13 with or without CX at GD14. DMSO, $n = 3$ mice per group; saline + CX, $n = 4$; MIA + CX, $n = 6$. (G) Iba1+ microglial cells (arrowheads) in the cortex of PD30 saline + CX and MIA + CX offspring (blue, nuclear marker DAPI). Cortical region depicted in G, Inset. (Scale bar, 20 μm.) (H) Iba1+ cells density in saline and MIA PD30 cortex with or without CX at GD14. (B, D, and H) $n = 4$ mice per group. Data are presented as mean ± SEM. ns, not significant. **$P < 0.01$, one-way ANOVA with Tukey's multiple comparison test; ***$P < 0.001$, one-way ANOVA with Tukey's multiple comparison test.

striatum (*SI Appendix*, Fig. S11D). As expected from the cellular rescue, CX treatment prevented the gestational MIA-mediated increase of Gd-DTPA distribution into the live fetal brain at GD15 (Fig. 3H). Taken together, histological, cellular, and functional data demonstrate that COX2 inhibition acutely blocked gestational MIA-induced disruption of fetal BBB within 24 h. Consequently, CX treatment also prevented the long-lasting effects of gestational MIA on postnatal offspring BBB function and behaviors. Pericyte coverage of endothelial cells was normal in MIA + CX PD30 offspring cortex (Fig. 4 A and B) and other brain regions (*SI Appendix*, Fig. S12). Expression of the vascular inflammation marker VCAM1 had also returned to normal in the cortex (Fig. 4 C and D) and other brain regions (*SI Appendix*, Fig. S13 A and B) of offspring from CX-treated mothers. Furthermore, MIA + CX PD30 and PD180 offspring displayed normal Gd-DTPA distribution into the cerebral cortex and other brain regions (Fig. 4 E and F and *SI Appendix*, Fig. S13C). Immunofluorescence intensity of the astrocytic end-feet marker AQP4 measured in adjacent sections of the PD30 cortex was not different

between groups (*SI Appendix*, Fig. S13 D and E). Consistent with the functional data, parenchymal microglia cell number and activation status were normal in the cortex (Fig. 4 G and H) and other regions (*SI Appendix*, Fig. S14) of MIA + CX PD30 offspring. Finally, CX treatment prevented the development of MIA-induced long-term behavioral deficits since both center activity in the OFT at PD30 (*SI Appendix*, Fig S15 A and B) and novel object recognition at PD180 (*SI Appendix*, Fig. S15C) were not different between the MIA + CX, saline, and saline + CX groups. These data suggest that increased COX2 activity in the fetal brain triggered by gestational MIA perturbs BBB development, which leads to long-lasting BBB hyperpermeability and brain inflammation.

Gestational MIA Increases COX2-Expressing Perivascular Microglia in the Fetal BBB. It is well established that COX2 expression is induced by inflammation in multiple cell types in the adult brain (29, 31, 32), but little is known about its expression, induction, and role during fetal development.
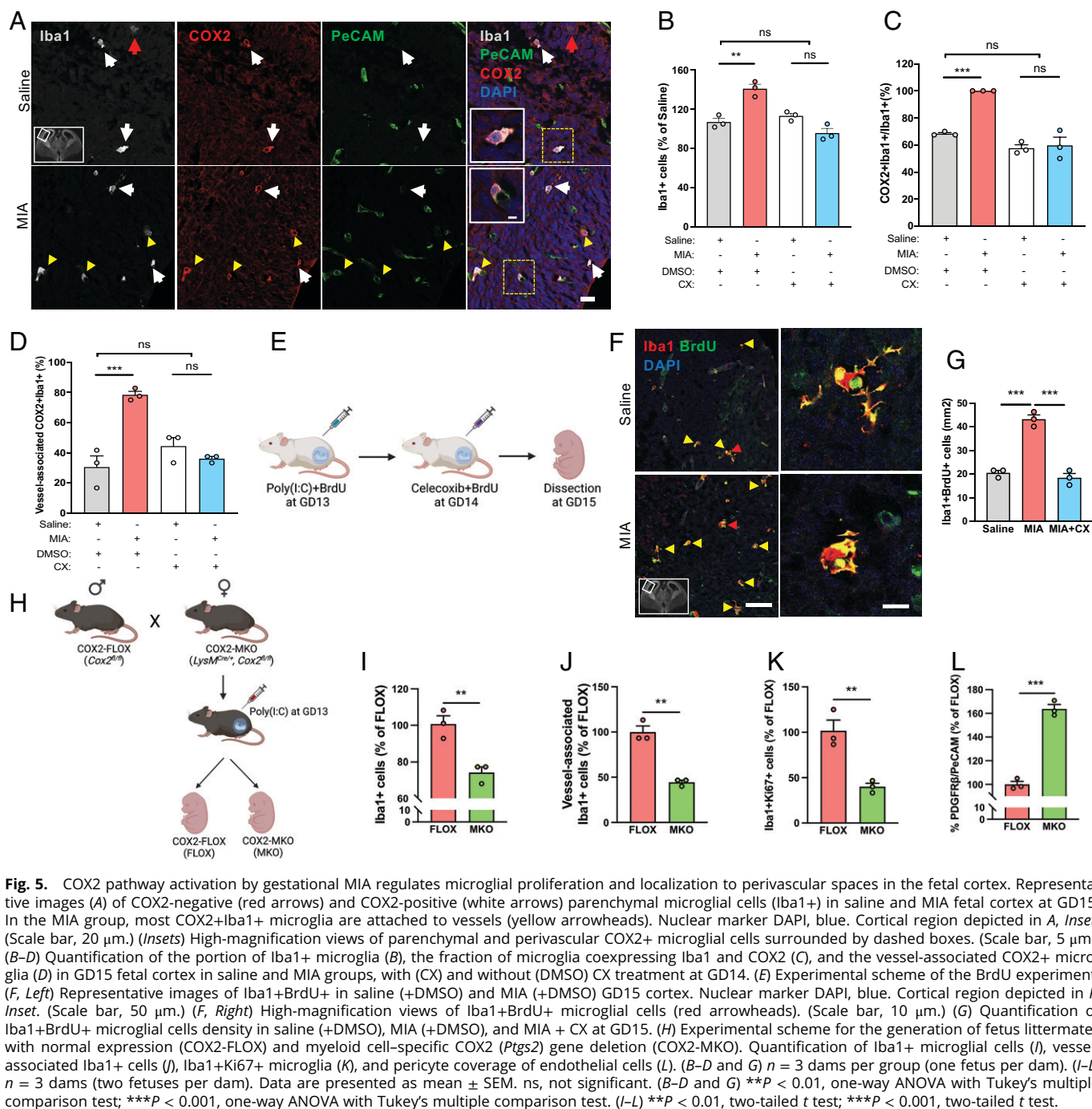
Fig. 5. COX2 pathway activation by gestational MIA regulates microglial proliferation and localization to perivascular spaces in the fetal cortex. Representative images (*A*) of COX2-negative (red arrows) and COX2-positive (white arrows) parenchymal microglial cells (Iba1+) in saline and MIA fetal cortex at GD15. In the MIA group, most COX2+Iba1+ microglia are attached to vessels (yellow arrowheads). Nuclear marker DAPI, blue. Cortical region depicted in *A*, *Inset*. (Scale bar, 20 μm.) (*Insets*) High-magnification views of parenchymal and perivascular COX2+ microglial cells surrounded by dashed boxes. (Scale bar, 5 μm.) (*B–D*) Quantification of the portion of Iba1+ microglia (*B*), the fraction of microglia coexpressing Iba1 and COX2 (*C*), and the vessel-associated COX2+ microglia (*D*) in GD15 fetal cortex in saline and MIA groups, with (CX) and without (DMSO) CX treatment at GD14. (*E*) Experimental scheme of the BrdU experiment. (*F*, *Left*) Representative images of Iba1+BrdU+ in saline (+DMSO) and MIA (+DMSO) GD15 cortex. Nuclear marker DAPI, blue. Cortical region depicted in *F*, *Inset*. (Scale bar, 50 μm.) (*F*, *Right*) High-magnification views of Iba1+BrdU+ microglial cells (red arrowheads). (Scale bar, 10 μm.) (*G*) Quantification of Iba1+BrdU+ microglial cells density in saline (+DMSO), MIA (+DMSO), and MIA + CX at GD15. (*H*) Experimental scheme for the generation of fetus littermates with normal expression (COX2-FLOX) and myeloid cell–specific COX2 (*Ptgs2*) gene deletion (COX2-MKO). Quantification of Iba1+ microglial cells (*I*), vessel-associated Iba1+ cells (*J*), Iba1+Ki67+ microglia (*K*), and pericyte coverage of endothelial cells (*L*). (*B–D* and *G*) $n = 3$ dams per group (one fetus per dam). (*I–L*) $n = 3$ dams (two fetuses per dam). Data are presented as mean ± SEM. ns, not significant. (*B–D* and *G*) **$P < 0.01$, one-way ANOVA with Tukey's multiple comparison test; ***$P < 0.001$, one-way ANOVA with Tukey's multiple comparison test. (*I–L*) **$P < 0.01$, two-tailed t test; ***$P < 0.001$, two-tailed t test.

Therefore, we next sought to identify in which cells COX2 expression is induced by gestational MIA in the fetal brain. We found that COX2 is constitutively expressed by a fraction ($46.3 \pm 1.2\%$ at GD13 + 48 h) of Iba1+ microglial cells in the fetal cortex (Fig. 5 *A* and *B*). Yet, consistent with increased COX2 enzymatic activity (Fig. 3*E*), cortical Iba1+/COX2+ cell number significantly increased 48 h post-MIA compared with controls (Fig. 5 *A* and *C*). At GD15, the majority ($77.1 \pm 22.6\%$) of COX2-expressing Iba1+ cells are perivascular in gestational MIA cortex, compared with $30.5 \pm 13.9\%$ in controls (Fig. 5*D*). The number of perivascular Iba1+/COX2+ cells returned to baseline 24 h after CX treatment in the MIA group (Fig. 5*D*). Furthermore, consistent with increased "activated" microglia (33, 34), the frequency of Iba1+ cells coexpressing CD45 or CD68 in GD15 cortex was increased ∼1.7- and

∼2.4-fold, respectively, in the gestational MIA group (CD45+/Iba1+ frequency: $30.4 \pm 10.2\%$ in saline controls to $53.8 \pm 17.1\%$ in MIA GD15 cortex; CD68+/Iba1+ number: 57.2 ± 15.9 cells/mm^2 in saline controls to 138.9 ± 23.5 cells/mm^2 in MIA GD15 cortex; both effects were reversed by CX treatment at GD14) (*SI Appendix*, Fig. S16 *A–E*). Furthermore, in the gestational MIA group, Iba1+/CD45+ cells also express COX2, and only very few cells are Iba1−CD45+COX2− in the GD15 cortex (*SI Appendix*, Fig. S16*C*). The increase in perivascular localization of Iba1+/COX2+ cells in the MIA group suggested that it may correspond to an increased number of perivascular macrophages (PVMs) or of infiltrating peripheral blood macrophages. To test the former possibility, we examined the expression of CD206 on fetal Iba1+ cells. The data (*SI Appendix*, Fig. S16 *F* and *G*) show 1) that there are

very few CD206+ cells in cortical regions investigated, 2) that MIA does not affect the number of CD206+ PVMs at GD15, and 3) that perivascular Iba1+ is CD206−. These data suggest that the increase in perivascular Iba1+/p2ry12+ microglia does not correspond to PVMs, and therefore, they are likely of parenchymal origin.

To further test if increased Iba1+ cell number resulted from increased proliferation rather than increased infiltration of peripheral macrophages, we injected subgroups of saline, MIA, and MIA + CX mothers with BrdU at GD13 and GD14 and measured the number of bromodeoxyuridine (BrdU)+ Iba1+ microglia in the fetal cortex at GD15. The data (Fig. 5 *F* and *G*) show a significant increase of BrdU+ Iba1+ microglia proliferation in the MIA group, which was prevented by CX injection at GD14. These observations overall suggest that COX2 activation in microglia is necessary to induce their proliferation, perivascular localization, and ultimately, fetal BBB disruption. To test this possibility, we performed conditional deletion of *COX2* (*Ptgs2*) gene specifically in myeloid cells using Cre recombinase expressed from the lysozyme M promoter (*LysM^{Cre}*) crossed to *COX2^{fl/fl}* mice (the crossing scheme in Fig. 5*H*). The pregnant dams used for MIA induction at GD13 carried litters composed of both littermate fetuses with normal COX2 expression (termed "FLOX") and with COX2 gene (termed "MKO") deleted in myeloid cells (including microglia). Confirming the specific deletion of COX2 in microglia, COX2-MKO GD15 littermates showed no detectable COX2 immunoreactivity in Iba1+ cells in the cortex after MIA, whereas COX2-FLOX littermates displayed the expected pattern of increased number and perivascular localization of Iba1+COX2+ microglia (*SI Appendix*, Fig. S17). The quantitative data show that 48 h after MIA induction, the number of Iba1+ microglia cells (Fig. 5*I*) in the fetal cortex from MKO fetuses is similar to saline controls but significantly lower compared with COX2-FLOX fetuses. Similarly, effects of MIA on perivascular localization (Fig. 5*J*) or proliferation (Fig. 5*K*) of Iba1+ cells in the GD15 fetal cortex are lower in COX2-MKO than COX2-FLOX fetuses. Furthermore, pericyte (PDGFRβ+) coverage of endothelial cells (PeCAM+) in the fetal cortex from COX2-MKO fetuses exposed to MIA is similar to saline controls and significantly higher than MIA-exposed COX2-FLOX fetuses (Fig. 5*L*).

These observations taken together show that MIA triggers a COX2-dependent increase in microglial proliferation and perivascular localization in the fetal cortex taking place between GD14 and GD15. This COX2-dependent activation of fetal microglia is associated with decreased pericyte coverage of fetal endothelial cells in the developing BBB.

Discussion

Our findings demonstrate the long-lasting influence of the intrauterine environment on brain function via early effects on cerebrovascular development. We found that gestational maternal inflammation in pregnancy disrupts fetal BBB formation via a COX2-dependent mechanism, leading to structural alterations and functional hyperpermeability of the offspring BBB that persist into adulthood. The data suggest that gestational MIA-induced failure of normal BBB formation is mediated by increased microglia proliferation and localization to the perivascular space of the fetal brain, a mechanism dependent on COX2 activity. The data support a process by which alteration of normal fetal BBB development results in chronic barrier hyperpermeability, leading to the well-documented adult offspring brain parenchymal inflammation and behavioral deficits induced by gestational MIA.

A striking observation in our study is that a single prenatal inflammatory insult, albeit severe given the amplitude of maternal proinflammatory cytokines induction (35), is sufficient to induce long-lasting BBB dysfunction in the offspring. Since we induced the inflammatory insult early in utero, several days before the BBB is fully functional (36–38), it is likely that disruption of normal fetal BBB development led to the adult phenotypes. Indeed, we found that as early as 48 h after gestational MIA induction, there is an increase of Gd-DTPA tracer distribution into the fetal brain, suggesting that the nascent BBB might already be compromised. This possibility is supported by histological data showing MIA-induced decreased pericyte–endothelium coverage and increased microglia cell number in the fetal brain, phenotypes like those observed later at PD30 and PD180. We sought to determine which immune signals alter the normal coupling of pericytes to blood vessels, a key step of BBB formation taking place around the time of gestational MIA induction (GD13 to GD15) (37–39). Some studies of gestational MIA have suggested direct effects of maternal cytokines on fetal neuronal development (40, 41), even though the possibility that these maternal blood-borne molecules can reach the fetal brain in sufficient amounts to drive abnormal development was not clearly demonstrated. Although we observed an expected transient surge in maternal blood cyto-/chemokines concentration within 6 h of poly(I:C) injection, we did not detect any significant change in IL-6, TNFα, and MCP-1 protein tissue concentration in the fetal brain 6, 28, or 48 h after gestational MIA induction. The lack of maternal cytokines diffusion into the fetal brain observed in our study suggests that these maternally derived molecules, at least IL-6, TNFα, and MCP-1, are not directly responsible for the rapid fetal BBB disruption. Instead, we found that the immune mediator PGE2 is significantly increased in the fetal brain 28 h after gestational MIA induction. PGE2 is a product of arachidonic acid metabolism by COX2 and mPGES1 enzymes, the former being highly inducible in multiple tissues in response to inflammation (30). PGE2 was shown to induce increases in peripheral microvessel endothelial cell permeability (42) and has been linked to alterations in BBB integrity during inflammation in the adult central nervous system (43, 44). Although PGE2 is only one of multiple prostaglandins downstream of prostaglandin H2 (PGH2) generated by COX2 pathway activation, its elevated concentration in the fetal brain and the elevation of COX2, but not COX1, enzymatic activity together point to this pathway involvement in MIA response. However, the inflammation-dependent induction and more generally, the role of PGE2 and COX2 in the fetal brain are less known. Several prostanoid receptors (EP1 to EP4) are expressed prenatally in various tissues (45) and could be mediating PGE2 effects, however their expression in the fetal brain, including components of the developing BBB, remains to be investigated. Based on the fetal brain PGE2 tissue concentration increase measured 28 h after gestational MIA induction, we hypothesized that COX2 activation in the fetal brain itself could be a critical mediator of gestational MIA effects on fetal BBB formation and maturation. Consistent with this possibility, we found that blocking COX2 activity with CX 24 h after gestational MIA induction, when maternal serum cytokines have returned to baseline, prevents both the acute (prenatal) and long-lasting effects of gestational MIA on BBB structure and function in the offspring. CX treatment itself might be associated with developmental toxicities [e.g., high-dose CX in third trimester pregnant humans and fetal lambs can induce constriction of ductus arteriosus (46, 47)]; however, there is no evidence of developmental toxicity or teratogenicity associated with CX treatment in mice.

These data indicate that COX2 activity in the fetal brain is critical in the early phase of gestational MIA-induced disruption of BBB development. The possibility that maternally derived PGE2 contributes to fetal brain effects is unlikely because we did not detect an increase in maternal serum PGE2 at any time point, and in vivo studies have shown that PGE2 is rapidly degraded by the lung and therefore, has a short half-life (∼30 s) (48) in adults.

In the adult brain, COX2 expression in several cell types is almost exclusively induced by inflammation; in the fetal brain, however, it is unclear if and where COX2 is expressed, except for two reports of COX2 induction in perivascular cells in response to in utero inflammation (49, 50). We observed that, concomitant to brain PGE2 increase, a fraction of microglial cells coexpressing Iba1 and COX2 is significantly increased by gestational MIA. CX treatment, after the surge in maternal serum cytokines (GD14), fully prevents gestational MIA effects on cerebrovascular dysfunction. Since CX can cross the placenta (46), it can target COX2-expressing cells, which in the fetal MIA brain, appear limited to Iba1+ microglia. Specificity of the effect is also supported by data showing that knocking out *Ptgs2* specifically in myeloid cells (including microglia) similarly to CX prevents MIA effects on fetal BBB disruption. Overall, the findings suggest that COX2 expression and possibly, PGE2 production by microglia in the fetal brain are a necessary early trigger of BBB disruption. There is evidence that microglial cells express COX2 in response to inflammation in the adult brain (51). Interestingly, the release of PGE2 was shown to drive BBB disruption in adults, possibly via matrix metallopeptidase 9 (MMP-9) production, leading to reduction in pericyte–endothelium coupling and degradation of cellular junctions (52, 53). Furthermore, unlike the adult, COX2 protein is constitutively expressed in several cell types of the normal fetal brain, in the absence of overt inflammation. It is possible that molecular pathways associated with degeneration and remodeling in the adult are constitutively active in the fetal brain when the BBB is in an active growth phase (36, 37, 39). In this context, gestational MIA could push the activation of normal developmental pathways above a destructive threshold. Nevertheless, the precise role of COX2 expressing microglia in mediating inflammation effects on fetal BBB formation is unknown. In normal postnatal development, up to ∼30% of all resting microglia are perivascular (54). This is comparable with the fraction of perivascular COX2+/Iba1+ microglia (∼30.5%) we measured in the cortex from saline-exposed fetuses. The fraction of COX2-expressing microglia perivascular localization in GD15 brains was significantly increased (∼1.6-fold) by gestational MIA. The increase in perivascular localization of Iba1+/COX2+ cells in the MIA group suggested that it may correspond to an increased number of CD206-expressing PVMs or of infiltrating peripheral blood macrophages. However, the very small number of CD206+ cells in cortical regions investigated at GD15 was not affected by MIA, and perivascular Iba1+ was CD206 negative. These data suggest that the increase in perivascular microglia does not correspond to PVMs but rather, originated from increased proliferation of parenchymal microglia migrating toward blood vessels. Furthermore, consistent with the increased activated microglia phenotype (33, 34), the frequency of Iba1+ cells coexpressing CD45 or CD68 in GD15 cortex was increased in the gestational MIA GD15 cortex; both effects were reversed by CX treatment at GD14. The rapid (within 24 h) CX inhibition of gestational MIA effects on microglia phenotypes and fetal BBB formation suggests that COX2 expression in microglial cells could be responsible for their proliferation, activation, and/or localization. The conditional deletion of *COX2* (*Ptgs2*) gene specifically

in myeloid cells showed that MIA effects on microglia proliferation and perivascular localization are dependent on COX2 expression in these cells. Furthermore, deletion of the COX2 gene from myeloid cells in the fetus prevented MIA-induced reduction in pericyte coverage of endothelial cells in the fetal cortex. We did not observe COX2 expression in endothelial cells in the fetal or adult brain after MIA. Although we cannot exclude that endothelial cell might express COX2 at other time points after MIA induction, we clearly observe that microglia are the main cell type expressing high levels of this enzyme in the brain and that knocking out COX2 specifically in myeloid cells, including microglia, is sufficient to prevent MIA effects on BBB. Therefore, we propose that MIA-induced fetal BBB disruption is mainly driven by the COX2-dependent microglial proliferation, activation, and migration toward perivascular spaces.

Other than potential implications in the etiology of neurodegenerative and aging-associated disorders, maternal infection during pregnancy is a known environmental risk factor for neurodevelopmental disorders, including schizophrenia and autism, in both primate and rodent offspring (55). Additionally, an emerging etiological aspect common to several neurological and neurodevelopmental disorders is BBB dysfunction. For instance, disrupted BBB function was demonstrated or suggested in schizophrenia (56) and autism (57) as well as aging-related disorders, such as AD (14). Interestingly, although COX2 inhibition did not provide therapeutic protection from AD burden in aging patients showing chronic cerebrovascular inflammation (58), it shows potential in early-phase treatment of depression and schizophrenia (59). Looking at even earlier time points in disease etiology, our data suggest an important role of this enzymatic pathway in the very early, inflammation-induced disruption of BBB formation via decreased pericyte coverage of endothelial cells leading to dysfunction across the life span. These findings raise interesting prospects for understanding the mechanisms driving the long-term consequences of inflammation in pregnancy on offspring brain function.

Materials and Methods

Animals. CD-1 timed pregnant mice were purchased from Charles River Laboratory. COX2-MKO (*LysM^{Cre/+}Cox2^{fl/fl}*) and COX2-FLOX (*Cox2^{fl/fl}*) (Fig. 5*H*) mice were gifts from Srinivasa Reddy and David Meriwether (UCLA, Los Angeles, CA) (60). COX2-MKO mice expressing Cre recombinase from the lysozyme M promoter were crossed to COX2-FLOX mice to generate myeloid cell-specific knockout COX2 embryos. Conditional COX2-MKO and control COX2-FLOX embryos were littermates. Mice were group housed (two to five per cage) in specific pathogen-free conditions in the animal facility, were kept on a 12-h/12-h light-dark cycle with lights on at 6 AM, and had ad libitum access to food and water. Since sex had no significant effect on behavior and MRI measures (in the text), both male and female offspring mice (pre- and postnatal) were used in all experiments, and the number of males and females in each group was balanced. All experiments were performed according to the NIH *Guide for the Care and Use of Laboratory Animals* (61) and approved by the Institutional Animal Care and Use Committee at the University of Southern California.

Gestational MIA. On GD13, pregnant CD-1 and COX2-MKO mice were weighted and intraperitoneally (i.p.) injected once with a single dose of poly(I:C) (10 mg/kg using 10 μL/g per pregnant dam, P9582; Sigma) or 0.9% sterile saline vehicle. Subsets of pregnant mice were injected once daily with BrdU (50 mg/kg, i.p.; Sigma-Aldrich; B5002) for 2 consecutive days at GD13 and GD14. A total of 90 dams were used in prenatal studies. Since poly(I:C) reagent composition and manufacturing origin influence MIA severity and phenotypes (62, 63), we performed additional assessments of MIA effects in CD-1 mice. Maternal weight was recorded from GD13 to GD18 each day after poly(I:C) injection. Birth date, litter size, sex ratio, and birth weight were obtained after birth. All dams were returned to their home cages immediately after injection. Dams were

Table 1. Number of litters used throughout the study

	No. of litters (total)
Prenatal imaging and tissue collection	
MRI	33 dams (1 to 3 fetuses per dam)
Immunohistochemistry	33 dams (from the GD15 MRI group; 1 fetus per dam)
Cytokine analyses	18 dams (1 fetus per dam)
PGE2 and COX1/2 activity measures	12 dams (1 fetus per dam)
Transgenic mice	3 dams (1 COX2-MKO and 1 COX2-FLOX fetus littermates per dam)
Postnatal imaging, behavior, and tissue collection	
PD30	15 dams (1 male and 1 female per dam)
PD180	6 dams (1 male and 1 female per d am)

randomly assigned to the following groups: 1) live MRI 48 h after injection followed by 2) either blood, placenta, and fetal brain collection 24 to 48 h after injection or normal continuation of pregnancy to generate postnatal and adult offspring (Table 1). Pups were weaned at PD21, at which time they were group housed (maximum of five per cage) with same-sex littermates. At PD30, pups taken from different litters for each treatment group were used for live MRI and behavioral assessment and culled for histological analyses.

Genotyping. DNA was extracted from fresh or frozen tissue by heating at 95 °C for 2 h in a 26 mM NaOH and 0.2 mM ethylenediaminetetraacetic acid (EDTA) solution. Sample tubes were flicked every 30 min during the heating process and cooled on ice for 10 min afterward. An equal volume of 40 mM tris(hydroxy-methyl)aminomethane (Tris)·HCl solution was added to the samples to neutralize the DNA solutions.

LysMcre PCR was run using Taq Plus 2X Master Mix Red (D124R; Lamda Biotech) and COX2-flox PCR using Kapa 2G HotStart Taq 2X Ready Mix with dye (KK5609; Roche Sequencing and Life Science, Kapa Biosystems). Additional $MgCl_2$ was added at a final concentration of 25 mM, and 6.5% (vol/vol) glycerol was used in the COX2-flox PCR mixture. Specific temperature and cycling conditions are listed in Table 2.

Drugs. CX (PZ0008; Sigma), a COX2 inhibitor, was dissolved in 20% DMSO with saline and administered i.p. (20 mg/kg) once 24 h after poly(I:C) injection. Control animals received the vehicle alone.

Blood Cytokines Measure. Separate cohorts were euthanized 6, 28, and 48 h after poly(I:C) injection to measure cytokines and chemokines in maternal blood serum and fetal brain. Cytokine and chemokine measurements were assayed using the Luminex multiplexing cytokine suspension array technology. Measurements of IL-6, TNFα, and MCP-1 were analyzed using a MilliPlex MAP mouse high-sensitivity cytokine/chemokine magnetic bead panel (MHSTCMAG-70K; MilliporeSigma). Plates were read on a Bio-Plex 200 System using Bio-Plex Manager software version 6.2 (BioRad). Five parameter logistic regression algorithms were used to determine analyte concentrations based on provided standards and averages from samples run in triplicate wells.

PGE2 and COX Activity Measures. Fetal brains were quickly harvested 28 and 48 h after poly(I:C) injection, rinsed in ice-cold phosphate buffer solution (PBS), and frozen in liquid nitrogen. PGE2 tissue concentration was measured using a

PGE2 enzyme-linked immunosorbent assay (ELISA) kit (R&D Systems; catalog no. KGE004B). COX activity was measured using a COX Activity Assay Kit (Cayman; catalog no. 760151). Samples were processed according to manufacturer instructions; briefly, tissue was transferred to an Eppendorf tube with 200 μL of lysate buffer (protease inhibitor mixture in PBS) and then, homogenized using a plastic tissue homogenizer. PGE2 concentrations and COX enzymatic activity were normalized to total protein concentration measured by bicinchoninic acid (BCA) assay and expressed as percentage of saline. Each sample was assayed in triplicate.

Behavioral Measures.
OFT. PD180 and PD30 offspring were individually placed in an OFT arena (50- × 50- × 30-cm walls), and their activity was recorded using a video camera (Canon Vixia HF R500) over 30 min. Distance traveled and the time spent in the central zone (20 × 20 cm) as well as the total distance and global activity were measured using a video tracking system (Smart v3.0 software; Harvard Apparatus).
Novel object recognition. For the novel object recognition task, mice were habituated to a black plastic cage (25 cm³) for 10 min for 3 d and exposed 3 times to the two objects trial. Mice were placed in a corner to minimize spatial memory confounds. In the training, two identical approximately 5 × 5 cm objects were placed in the cage, and the mouse was allowed to explore for 5 min, which was recorded. Two hours later, the mouse was placed back in the same cage, in which one of the objects used in the training was replaced by a novel object and allowed to explore for another 5 min. Total duration of time spent to explore familiar or novel objects was measured. The exploratory preference was calculated as a ratio of time spent exploring the novel object over the total time exploring both objects.

Immunohistochemistry. Fetal brains were dissected at GD15 and fixed with 4% paraformaldehyde (PFA) in PBS overnight at 4 °C. PD30 mice were deeply anesthetized and transcardially perfused with 0.01 M PBS (pH 7.0) followed by 4% PFA in PBS, and the brain was postfixed with 4% PFA in PBS overnight at 4 °C. After fixation, the brains went through gradient dehydration in 10, 20, and 30% sucrose solutions for 24 h each, and then, they were embedded in optimal cutting temperature compound (OCT), cut into 20-μm-thick sections with cryostat (CM3050S; Leica), mounted onto superfrost plus slides, and stored at −80 °C until analyses.

Immunohistochemistry was performed as previously described (64–67). Sections were permeabilized in blocking solution containing 0.1% Triton X-100 and 2% fetal bovine serum in PBS for 2 h at room temperature and incubated in a humidified chamber with primary antibodies overnight, followed by secondary

Table 2. Primers and PCR conditions for genotyping conditional COX2-MKO mice

PCR and primer	Sequence	PCR condition
LysM$^{Cre/+}$		
LysMcre forward primer	5′-CTT GGG CTG CCA GAA TTT CTC-3′	94 °C 20 s, 60 °C 20 s, 70 °C 30 s,
LysMcre reverse primer 1	5′-CCT CAC CCC AGC ATC TCT AAT TC-3′	repeat 39 cycles
LysMcre reverse primer 2	5′-ATC ACT CGT TGC ATC GAC CGG TAA-3′	
Cox2$^{fl/fl}$		
COX2-FLOX forward primer	5′-TGC CCT TGT TGT TGT TG-3′	94 °C 30 s, 65 °C 1 min, 68 °C 30 s,
COX2-FLOX wild-type reverse primer	5′-GTT GGG CAG TCA TCT GCT AC-3′	repeat 10 cycles (−0.5 °C per cycle),
COX2-FLOX mutant reverse primer	5′-TGG ACG TAA ACT CCT CTT CAG AC-3′	94 °C 30 s, 60 °C 30 s, 72 °C 2 min, repeat 28 cycles

antibodies incubation for 2 h at room temperature. For SMA staining, an incubation step in Tyramide Signal Amplification-Cy3 solution (1:100; PerkinElmer; NEL7441B001KT) for 30 min was performed. Primary antibodies used included the following: PeCAM (CD31; rat anti-PeCAM, 1:30; BD Biosciences; 550274; hamster anti-CD31, 1:1,000; Millipore; MAB1398Z), mouse anti-SMA (1:100; Dako; M0851), rat anti-VCAM1 (1:200; Bio-Rad; MCA2297GA), Iba1 (rabbit anti-Iba1, 1:500; WAKO; 019-19741; goat anti-Iba1, 1:200; Novus Biological; NB100-1028), rabbit anti-TMEM119 (1:500; Abcam; Ab209064), goat anti-PDGFRβ (1:100; R&D Systems; AF-1042), rat anti-P2ry12 (1:100; BioLegend; 848002), Dylight 488–conjugated lectin (1:200; Vector Labs; DL-1174), goat anti-CD13 (1:100; R&D System; AF2335), COX2 (rabbit anti-COX2, 1:200; Abcam; Ab15191; rabbit anti-COX2, 1:150; Cayman; 160126), rat anti-CD68 (1:200; Biorad; MCA1957GA), rat anti-CD45 (1:50; BD Biosciences; 550539), rabbit anti-BrdU (1:200; CST; 5292), mouse anti-Ki67 (1:200; CST; 9449), mouse Claudin 5-Alexa 488 (1:100; ThermoFisher; 352588), rabbit anti-ZO1 (1:100; ThermoFisher; 40-2200), rabbit anti-AQP (1:500; Millipore; AB3594), and rat anti-CD206-Biotin (1:200; Biorad; MAC2235B). Secondary antibodies (1:800; Jackson ImmunoResearch), raised in donkey, included the following: anti-rat Alexa 488, anti-rat Rhodamine Red, anti-rabbit Rhodamine Red, anti-rabbit Alexa 488, anti-rabbit Alexa 647, anti-goat Alexa 488, anti-goat Rhodamine Red, anti-goat Alexa 647, goat anti-hamster Alexa 488, rabbit anti-mouse horseradish peroxidase (HRP), and DyLight 549 streptavidin (1:500; Vector Labs; SA-5549). Sections were coverslipped with Prolong Gold (Vector) and imaged using a Zeiss Axioimager 2 microscope and a confocal microscope (LSM800; Zeiss); for comparisons between groups within staining batches, all image acquisition settings were kept constant.

Image Quantification and Analysis. In each mouse, three regions of interest (ROIs; e.g., the parietal/somatosensory cortex region of the fetal and PD30 brain, thalamus, and striatum) were analyzed in four nonadjacent sections (~100 μm apart) and averaged per animal. Quantification of pericyte coverage of endothelial cells was done using ImageJ according to the method described in ref. 68. Briefly, black and white 32-bit images for PDGFRβ/PeCAM, SMA/PeCAM, PDGFRβ/lectin, and CD13/lectin were thresholded using the Otsu plug-in. The area ratios of SMA or PDGFRβ and PeCAM (prenatal tissue) and CD13 or PDGFRβ and lectin (postnatal tissue) were used to calculate pericyte-like cell coverage endothelial cell. For lectin, PeCAM, Claudin 5, ZO1, and AQP4, images were analyzed using quantitative density measures as previously described (67). For vessel diameter, we created a maximum intensity projection of a 30-μm optical stack, and 200-μm lectin- and PeCAM-positive segments were selected randomly for diameter measurements. For each vessel, we did four measurements 50 μm apart as described in refs. 23 and 68. For microglia and macrophages assessment, Iba1, Iba1/COX2, Iba1/CD45, Iba1/TMEM119, Iba1/P2ry12, Iba1/CD68, Iba1/BrdU, and Iba1/Ki67 double-positive cells and Iba1/COX2/CD45 triple-positive cells in similar ROIs were counted manually using the Leica Microscope Imaging Software and normalized per squared millimeter. PVMs/perivascular microglia were quantified by counting the number of CD206+ and Iba1+ COX2+ cells/cytoplasm associated (making contact) with PeCAM+ blood vessels and expressed as the ratio to the total number of Iba1+COX2+ cells in each ROI.

MRI. All MRI scans were performed using our MR Solutions 7T PET MR system (bore size of ~24 cm, up to 600 mT·m^{-1} maximum gradient strength and a 20-mm–internal diameter quadrature bird cage mouse head coil). Mice were anesthetized by 1 to 1.2% isoflurane in air. Respiration rate (80.0 ± 10.0 breaths per minute) and body temperature (36.5 ± 0.5 °C) were monitored during the experiments, as described previously (17).

Prenatal MRI. For abdominal scans, the scans were collected with respiratory gating in the following order. 1) Pre- and postgadolinium contrast coronal T1-weighted imaging (two-dimensional [2D] fast spin echo [FSE], time repetition [TR]/time echo [TE] 1,150/11 ms, echo train length of four, six averages, 20 slices, slice thickness of 400 μm, in-plane resolution 140 × 140 μm^2) was used to assess blood–placenta and blood–fetal brain barrier permeability. A bolus dose (140 μL) of 1.5 mmol·kg^{-1} Gd-DTPA (gadolinium diethylenetriamine pentaacetic acid diluted in saline 1:2) was injected into the tail vein. 2) T2-weighted imaging (2D FSE, TR/TE 3,010/45 ms, echo train length of seven, 25 slices, slice thickness of 1 mm, in-plane resolution 140 × 140 μm^2) was used to obtain anatomical images. Total imaging time was ~40 to 50 min per mouse depending upon respiratory triggering.

Postnatal MRI. For adult brain scans, the scans were collected in the following order: 1) T2-weighted imaging (2D FSE, TR/TE 4,900/45 ms, echo train length of seven, three averages, 40 slices, slice thickness of 400 μm, in-plane resolution 70 × 70 μm^2) to obtain anatomical images; 2) T2*w (2D gradient echo [GRE], TR/TE 415/5 ms, six averages, 28 slices, slice thickness of 500 μm, in-plane resolution 60 × 160 μm^2) to assess possible microbleeding events; 3) horizontal time of flight (TR/TE 25/3 ms, FA [flip angle] 45°, two averages, 64 slices, slice thickness of 230 μm, in-plane resolution 100 × 160 μm^2) to obtain angiography images; 4) precontrast T1-weighted using a variable flip angle (VFA) fast low-angle shot (FLASH) sequence (FA = 5°, 10°, 15°, 30°, and 45°, TE 4 ms, slice thickness of 1 mm, in-plane resolution 80 × 80 μm^2) followed by a dynamic series of 180 T1-weighted images with identical geometry and a temporal resolution of 5.1 s (FLASH, TR/TE 35/4 ms, FA 15°, two averages, two slices, slice thickness of 1 mm, in-plane resolution 80 × 80 μm^2). A bolus dose (140 μL) of 0.5 mmol·kg^{-1} Gd-DTPA (diluted in saline 1:6) was injected into the tail vein at a rate of 600 μL·min^{-1} using a power injector. DCE images were collected before and for 15 min after the injection. Total imaging time was ~50 min per mouse.

Molecular MRI was also performed on a subset of mice to assess vascular inflammation. As previously described (21), microparticles of iron oxide (MPIO; diameter of 1.08 μm) with p-toluenesulphonyl–reactive surface groups were covalently conjugated to purified monoclonal rat anti-mouse antibodies for VCAM1. Mice received intravenous injection of 0.25 mg/kg (equivalent Fe; 100 μL) of conjugated MPIOs for contrast-enhanced T2*w MRI. A three-dimensional (3D) FLASH sequence was used (TR/TE 200/12 ms, FA 24°, two averages, slice thickness of 100 μm, in-plane resolution 100 × 100 μm^2). Imaging was performed 5 min after particles administration and lasted for 30 min total.

MRI Analysis. To study fetal BBB permeability, we analyzed the difference in mean SI between the pre- and postcontrast T1-weighted images using specific ROIs in all studied groups. Fetal brain images were manually segmented on high-resolution T2-weighted images using ImageJ.

To study BBB permeability in the offspring, T1 relaxation times were first estimated using the VFA method, prior to Gd-DTPA injection, with a series of FLASH images with varying FA and constant TR and TE using the standard saturation recovery equation, as we described previously (17, 23). Then, postprocessing of the collected DCE MRI data was performed using in-house DCE processing software (Rocketship) implemented in MATLAB (69). The unidirectional blood-to-brain transfer constant, K_{trans}, to intravenously injected gadolinium-based contrast agent was determined in primary somatosensory cortex, thalamus, and striatum in mice using a modified method, as we reported in both humans (11, 70) and mice (17, 23) with the postprocessing Patlak analysis. We determined the arterial input function (AIF) in each mouse from the common carotid artery, as we also reported previously (17, 23). The total tracer concentration in the tissue, C_{tissue} (t), can be described as a function of the arterial vascular concentration C_{AIF} (t), the intravascular blood volume v_p, and the BBB permeability transfer constant K_{trans} that represents the flow of the tracer from the intravascular to the extravascular space using Eq. **1**:

$$C_{tissue}(t) = K_{trans} \int_0^t C_{AIF}(\tau)d\tau + v_p . C_{AIF}(t). \qquad [1]$$

For endothelial activation through VCAM1 expression, all T2*w images presented in this study are the minimum-intensity projection of three consecutive slices (yielding a Z resolution of 300 μm). Signal void quantification was determined using automatic Otsu thresholding in ImageJ as previously published (21). Results are presented as volume of MPIO-induced signal void divided by the volume of the structure of interest (in percentage). The selected ROIs are whole brain, primary somatosensory cortex, thalamus, and striatum.

Statistics. Statistical analyses were performed using GraphPad Prism 8.0 software. Results from histological experiments were compared using the unpaired two-tailed *t* test, one-way ANOVA followed by Tukey's multiple comparison analysis, or two-way ANOVA followed by Bonferroni's multiple comparisons analysis, depending on the number of variables included in the comparison. In behavioral and MRI experiments, results were compared using the unpaired two-tailed *t* test (between two groups) and one-way ANOVA followed by Tukey's multiple comparison when comparing more than two groups. Test type and levels of statistical significance are indicated in the figures. All data are represented as mean ± SEM.

1. R. E. Kneeland, S. H. Fatemi, Viral infection, inflammation and schizophrenia. *Prog. Neuropsychopharmacol. Biol. Psychiatry* **42**, 35–48 (2013).
2. J. Boulanger-Bertolus, C. Pancaro, G. A. Mashour, Increasing role of maternal immune activation in neurodevelopmental disorders. *Front. Behav. Neurosci.* **12**, 230 (2018).
3. D. Krstic *et al.*, Systemic immune challenges trigger and drive Alzheimer-like neuropathology in mice. *J. Neuroinflammation* **9**, 151 (2012).
4. X. Y. Li *et al.*, Inflammatory insult during pregnancy accelerates age-related behavioral and neurobiochemical changes in CD-1 mice. *Age (Dordr.)* **38**, 59 (2016).
5. S. B. Gumusoglu, H. E. Stevens, Maternal inflammation and neurodevelopmental programming: A review of preclinical outcomes and implications for translational psychiatry. *Biol. Psychiatry* **85**, 107–121 (2019).
6. S. Smolders, T. Notter, S. M. T. Smolders, J. M. Rigo, B. Brône, Controversies and prospects about microglia in maternal immune activation models for neurodevelopmental disorders. *Brain Behav. Immun.* **73**, 51–65 (2018).
7. I. Knuesel *et al.*, Maternal immune activation and abnormal brain development across CNS disorders. *Nat. Rev. Neurol.* **10**, 643–660 (2014).
8. K. A. Walker, B. N. Ficek, R. Westbrook, Understanding the role of systemic inflammation in Alzheimer's disease. *ACS Chem. Neurosci.* **10**, 3340–3342 (2019).
9. V. V. Giridharan, F. Masud, F. Petronilho, T. Dal-Pizzol, T. Barichello, Infection-induced systemic inflammation is a potential driver of Alzheimer's disease progression. *Front. Aging Neurosci.* **11**, 122 (2019).
10. J. Paul, S. Strickland, J. P. Melchor, Fibrin deposition accelerates neurovascular damage and neuroinflammation in mouse models of Alzheimer's disease. *J. Exp. Med.* **204**, 1999–2008 (2007).
11. A. Montagne *et al.*, Blood-brain barrier breakdown in the aging human hippocampus. *Neuron* **85**, 296–302 (2015).
12. A. Montagne, Z. Zhao, B. V. Zlokovic, Alzheimer's disease: A matter of blood-brain barrier dysfunction? *J. Exp. Med.* **214**, 3151–3169 (2017).
13. H. J. van de Haar *et al.*, Blood-brain barrier leakage in patients with early Alzheimer disease. *Radiology* **281**, 527–535 (2016).
14. M. D. Sweeney, Z. Zhao, A. Montagne, A. R. Nelson, B. V. Zlokovic, Blood-brain barrier: From physiology to disease and back. *Physiol. Rev.* **99**, 21–78 (2019).
15. A. P. Sagare *et al.*, Pericyte loss influences Alzheimer-like neurodegeneration in mice. *Nat. Commun.* **4**, 2932 (2013).
16. C. Samaey, A. Schreurs, S. Stroobants, D. Balschun, Early cognitive and behavioral deficits in mouse models for tauopathy and Alzheimer's disease. *Front. Aging Neurosci.* **11**, 335 (2019).
17. A. Montagne *et al.*, Pericyte degeneration causes white matter dysfunction in the mouse central nervous system. *Nat. Med.* **24**, 326–337 (2018).
18. H. Thurgur, E. Pinteaux, Microglia in the neurovascular unit: Blood-brain barrier-microglia interactions after central nervous system disorders. *Neuroscience* **405**, 55–67 (2019).
19. A. Varatharaj, I. Galea, The blood-brain barrier in systemic inflammation. *Brain Behav. Immun.* **60**, 1–12 (2017).
20. M. Gauberti, A. Montagne, A. Quenault, D. Vivien, Molecular magnetic resonance imaging of brain-immune interactions. *Front. Cell. Neurosci.* **8**, 389 (2014).
21. A. Montagne *et al.*, Ultra-sensitive molecular MRI of cerebrovascular cell activation enables early detection of chronic central nervous system disorders. *Neuroimage* **63**, 760–770 (2012).
22. R. D. Bell *et al.*, Pericytes control key neurovascular functions and neuronal phenotype in the adult brain and during brain aging. *Neuron* **68**, 409–427 (2010).
23. A. M. Nikolakopoulou *et al.*, Pericyte loss leads to circulatory failure and pleiotrophin depletion causing neuron loss. *Nat. Neurosci.* **22**, 1089–1098 (2019).
24. D. Attwell, A. Mishra, C. N. Hall, F. M. O'Farrell, T. Dalkara, What is a pericyte? *J. Cereb. Blood Flow Metab.* **36**, 451–455 (2016).
25. D. A. Hartmann *et al.*, Brain capillary pericytes exert a substantial but slow influence on blood flow. *Nat. Neurosci.* **24**, 633–645 (2021).
26. R. Calvello *et al.*, Novel selective COX-1 inhibitors suppress neuroinflammatory mediators in LPS-stimulated N13 microglial cells. *Pharmacol. Res.* **65**, 137–148 (2012).
27. S. Schepanski, C. Buss, I. L. Hanganu-Opatz, P. C. Arck, Prenatal immune and endocrine modulators of offspring's brain development and cognitive functions later in life. *Front. Immunol.* **9**, 2186 (2018).
28. P. H. Patterson, Immune involvement in schizophrenia and autism: Etiology, pathology and animal models. *Behav. Brain Res.* **204**, 313–321 (2009).
29. S. H. Choi, S. Aid, F. Bosetti, The distinct roles of cyclooxygenase-1 and -2 in neuroinflammation: Implications for translational research. *Trends Pharmacol. Sci.* **30**, 174–181 (2009).
30. L. Minghetti, Cyclooxygenase-2 (COX-2) in inflammatory and degenerative brain diseases. *J. Neuropathol. Exp. Neurol.* **63**, 901–910 (2004).
31. W. A. Banks *et al.*, Lipopolysaccharide-induced blood-brain barrier disruption: Roles of cyclooxygenase, oxidative stress, neuroinflammation, and elements of the neurovascular unit. *J. Neuroinflammation* **12**, 223 (2015).
32. S. H. Choi, S. Aid, U. Choi, F. Bosetti, Cyclooxygenases-1 and -2 differentially modulate leukocyte recruitment into the inflamed brain. *Pharmacogenomics J.* **10**, 448–457 (2010).
33. C. Verney, A. Monier, C. Fallet-Bianco, P. Gressens, Early microglial colonization of the human forebrain and possible involvement in periventricular white-matter injury of preterm infants. *J. Anat.* **217**, 436–448 (2010).
34. J. Lier, W. J. Streit, I. Bechmann, Beyond activation: Characterizing microglial functional phenotypes. *Cells* **10**, 2236 (2021).
35. U. Meyer, Neurodevelopmental resilience and susceptibility to maternal immune activation. *Trends Neurosci.* **42**, 793–806 (2019).
36. M. Blanchette, R. Daneman, Formation and maintenance of the BBB. *Mech. Dev.* **138**, 8–16 (2015).
37. R. Daneman, L. Zhou, A. A. Kebede, B. A. Barres, Pericytes are required for blood-brain barrier integrity during embryogenesis. *Nature* **468**, 562–566 (2010).
38. B. Obermeier, R. Daneman, R. M. Ransohoff, Development, maintenance and disruption of the blood-brain barrier. *Nat. Med.* **19**, 1584–1596 (2013).
39. A. Ben-Zvi *et al.*, Mfsd2a is critical for the formation and function of the blood-brain barrier. *Nature* **509**, 507–511 (2014).
40. L. Hantsoo, S. Kornfield, M. C. Anguera, C. N. Epperson, Inflammation: A proposed intermediary between maternal stress and offspring neuropsychiatric risk. *Biol. Psychiatry* **85**, 97–106 (2019).
41. B. E. Deverman, P. H. Patterson, Cytokines and CNS development. *Neuron* **64**, 61–78 (2009).
42. K. S. Mark, W. J. Trickler, D. W. Miller, Tumor necrosis factor-α induces cyclooxygenase-2 expression and prostaglandin release in brain microvessel endothelial cells. *J. Pharmacol. Exp. Ther.* **297**, 1051–1058 (2001).
43. N. Tsao, H.-P. Hsu, H.-Y. Lei, TNFalpha-induced cyclooxygenase 2 not only increases the vasopermeability of blood-brain barrier but also enhances the neutrophil survival in *Escherichia coli*-induced brain inflammation. *Prostaglandins Other Lipid Mediat.* **57**, 371–382 (1999).
44. J. W. Schmidley, J. Dadson, R. S. Iyer, R. G. Salomon, Brain tissue injury and blood-brain barrier opening induced by injection of LGE2 or PGE2. *Prostaglandins Leukot. Essent. Fatty Acids* **47**, 105–110 (1992).
45. D. H. Wright *et al.*, Prostanoid receptors: Ontogeny and implications in vascular physiology. *Am. J. Physiol. Regul. Integr. Comp. Physiol.* **281**, R1343–R1360 (2001).
46. Y. Takahashi *et al.*, Cyclooxygenase-2 inhibitors constrict the fetal lamb ductus arteriosus both in vitro and in vivo. *Am. J. Physiol. Regul. Integr. Comp. Physiol.* **278**, R1496–R1505 (2000).
47. M. E. Østensen, J. F. Skomsvoll, Anti-inflammatory pharmacotherapy during pregnancy. *Expert Opin. Pharmacother.* **5**, 571–580 (2004).
48. I. Gomez, N. Foudi, D. Longrois, X. Norel, The role of prostaglandin E2 in human vascular inflammation. *Prostaglandins Leukot. Essent. Fatty Acids* **89**, 55–63 (2013).
49. E. Yan, M. Castillo-Meléndez, T. Nicholls, J. Hirst, D. Walker, Cerebrovascular responses in the fetal sheep brain to low-dose endotoxin. *Pediatr. Res.* **55**, 855–863 (2004).
50. S. Segal, C. Pancaro, I. Bonney, J. E. Marchand, Noninfectious fever in the near-term pregnant rat induces fetal brain inflammation: A model for the consequences of epidural-associated maternal fever. *Anesth. Analg.* **125**, 2134–2140 (2017).
51. A. C. de Oliveira *et al.*, Poly(I:C) increases the expression of mPGES-1 and COX-2 in rat primary microglia. *J. Neuroinflammation* **13**, 11 (2016).
52. M. R. Halliday *et al.*, Accelerated pericyte degeneration and blood-brain barrier breakdown in apolipoprotein E4 carriers with Alzheimer's disease. *J. Cereb. Blood Flow Metab.* **36**, 216–227 (2016).
53. E. Candelario-Jalil *et al.*, Cyclooxygenase inhibition limits blood-brain barrier disruption following intracerebral injection of tumor necrosis factor-α in the rat. *J. Pharmacol. Exp. Ther.* **323**, 488–498 (2007).
54. R. Grossmann *et al.*, Juxtavascular microglia migrate along brain microvessels following activation during early postnatal development. *Glia* **37**, 229–240 (2002).
55. M. Careaga, T. Murai, M. D. Bauman, Maternal immune activation and autism spectrum disorder: From rodents to nonhuman and human primates. *Biol. Psychiatry* **81**, 391–401 (2017).
56. S. Najjar *et al.*, Neurovascular unit dysfunction and blood-brain barrier hyperpermeability contribute to schizophrenia neurobiology: A theoretical integration of clinical and experimental evidence. *Front. Psychiatry* **8**, 83 (2017).
57. M. Fiorentino *et al.*, Blood-brain barrier and intestinal epithelial barrier alterations in autism spectrum disorders. *Mol. Autism* **7**, 49 (2016).
58. F. Jordan *et al.*, Aspirin and other non-steroidal anti-inflammatory drugs for the prevention of dementia. *Cochrane Database Syst. Rev.* **4**, CD011459 (2020).
59. N. Müller, COX-2 inhibitors, aspirin, and other potential anti-inflammatory treatments for psychiatric disorders. *Front. Psychiatry* **10**, 375 (2019).
60. D. Meriwether *et al.*, Apolipoprotein A-I mimetics mitigate intestinal inflammation in COX2-dependent inflammatory bowel disease model. *J. Clin. Invest.* **129**, 3670–3685 (2019).
61. National Research Council, *Guide for the Care and Use of Laboratory Animals* (National Academies Press, Washington, DC, ed. 8, 2011).
62. H. M. Kowash *et al.*, Poly(I:C) source, molecular weight and endotoxin contamination affect dam and prenatal outcomes, implications for models of maternal immune activation. *Brain Behav. Immun.* **82**, 160–166 (2019).
63. F. S. Mueller *et al.*, Influence of poly(I:C) variability on thermoregulation, immune responses and pregnancy outcomes in mouse models of maternal immune activation. *Brain Behav. Immun.* **80**, 406–418 (2019).
64. A. Bonnin *et al.*, A transient placental source of serotonin for the fetal forebrain. *Nature* **472**, 347–350 (2011).
65. A. Bonnin, M. Torii, L. Wang, P. Rakic, P. Levitt, Serotonin modulates the response of embryonic thalamocortical axons to netrin-1. *Nat. Neurosci.* **10**, 588–597 (2007).
66. N. Goeden *et al.*, Maternal inflammation disrupts fetal neurodevelopment via increased placental output of serotonin to the fetal brain. *J. Neurosci.* **36**, 6041–6049 (2016).
67. J. C. Velasquez *et al.*, In utero exposure to citalopram mitigates maternal stress effects on fetal brain development. *ACS Chem. Neurosci.* **10**, 3307–3317 (2019).
68. A. M. Nikolakopoulou, Z. Zhao, A. Montagne, B. V. Zlokovic, Regional early and progressive loss of brain pericytes but not vascular smooth muscle cells in adult mice with disrupted platelet-derived growth factor receptor-β signaling. *PLoS One* **12**, e0176225 (2017).
69. S. R. Barnes *et al.*, ROCKETSHIP: A flexible and modular software tool for the planning, processing and analysis of dynamic MRI studies. *BMC Med. Imaging* **15**, 19 (2015).
70. A. Montagne *et al.*, APOE4 leads to blood-brain barrier dysfunction predicting cognitive decline. *Nature* **581**, 71–76 (2020).